

# Direct and Energy-Transfer-Mediated Charge-Transfer State Formation and Recombination in Triangulene-Spacer-Perylenediimide Multichromophores: Lessons for Photovoltaic Applications

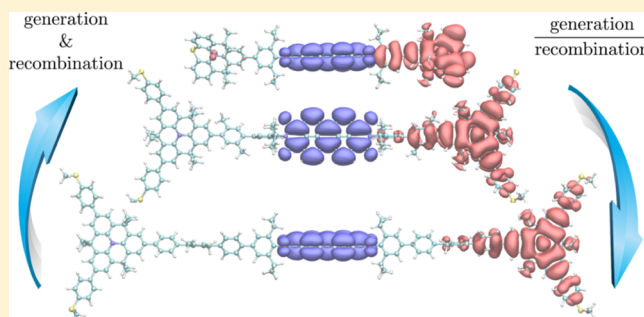
Ahmed H. Balawi,<sup>†,||</sup> Sebastian Stappert,<sup>‡,||</sup> Julien Gorenflot,<sup>†</sup> Chen Li,<sup>‡,§</sup> Klaus Müllen,<sup>\*,‡,§</sup> Denis Andrienko,<sup>\*,‡,‡</sup> and Frédéric Laquai<sup>\*,†,‡</sup>

<sup>†</sup>King Abdullah University of Science and Technology (KAUST), KAUST Solar Center (KSC), Physical Sciences and Engineering Division, Materials Science and Engineering Program, Thuwal 23955-6900, Kingdom of Saudi Arabia

<sup>‡</sup>Max Planck Institute for Polymer Research, Ackermannweg 10, D-55128 Mainz, Germany

## Supporting Information

**ABSTRACT:** We study the dynamics of primary photoexcitations in three symmetric donor–spacer–acceptor–spacer–donor multichromophores with increasing oligophenylene spacer length, following selective donor or acceptor excitation. Energy levels of the donor and acceptor moieties are tailored to facilitate splitting of the excited state into a lower-lying charge-transfer (CT) state, mimicking the functionality of a donor–acceptor interface for charge generation, thus resulting in long-lived charge separation. Ultrafast electronic energy transfer (ET) from the donor followed by fast hole (back)transfer from the acceptor populates the molecules' CT states. However, the CT efficiency is found to be close to unity, independent of the donor or acceptor photoexcitation. The ratio of CT and recombination rates, which reflects the population of CT states, increases with the oligophenylene spacer length for both direct hole transfer and hole transfer following ET, boosting the population of CT states under continuous excitation. We observe the population of high-lying “dark” excited states following ET from the donor to the acceptor. The “dark” states successively undergo CT and form CT states of higher energy, with decreased recombination rates, while maintaining the high charge generation efficiency. Changes in CT reaction rates are rationalized within the Marcus theory, with driving forces and reorganization energies evaluated by density functional theory and polarizable continuum models. The present study demonstrates the importance of energetically higher-lying states, which cannot be directly photoexcited yet are accessible through ET from local excited states. Similar processes are anticipated in other donor–acceptor systems, which allow for both energy and CT processes, such as bulk heterojunctions of the polymer and small-molecule donor/nonfullerene acceptor typically used in photovoltaic systems.



## INTRODUCTION

Photoinduced electronic energy-transfer (ET) and charge-transfer (CT) processes are of key interest in photosynthesis,<sup>1–3</sup> photocatalysis,<sup>4,5</sup> organic light-emitting diodes,<sup>6,7</sup> organic photovoltaic (OPV) cells,<sup>8–14</sup> and many related photophysical phenomena where long-distance charge separation is essential.<sup>15–19</sup> These processes are, however, rather intricate already in simple molecular donor–acceptor-type dyads,<sup>20–22</sup> where ET can proceed via the CT state, enabling fast ET between the donor and the acceptor units even with orthogonal transition dipoles.<sup>23</sup> Moreover, Förster or Redfield theories, which are successful in describing long-range ET, cannot rationalize it in small molecular dyads with large electronic couplings between the states.<sup>24–26</sup> The situation is even more complex in symmetric donor–acceptor–donor or

acceptor–donor–acceptor triads, where the symmetry of the CT state (quadrupolar vs dipolar) also depends on the strength of the electronic coupling between the donor and acceptor units and stabilization by the environment.<sup>27,28</sup> The molecular structure can therefore be used to control the CT mechanism by, for example, varying the length of the conjugated spacer, thereby controlling the coupling between the donor and acceptor in the multichromophore.<sup>16</sup>

The precise mechanism of CT and separation in donor–acceptor systems as nowadays used in organic solar cells (OSCs) is still a matter of debate. In this regard, an open

Received: May 30, 2019

Revised: June 17, 2019

Published: June 26, 2019

question is the optimum distance between the donor and acceptor that ensures complete CT and separation, while simultaneously suppressing CT state (geminate) recombination. Donor–spacer–acceptor molecules with varying spacer lengths between the donor and acceptor moieties are ideal test systems, as they allow to study the effect of donor–acceptor separation without the complexity of intermolecular interaction typical for a bulk heterojunction or even single-component OSCs.<sup>29–32</sup>

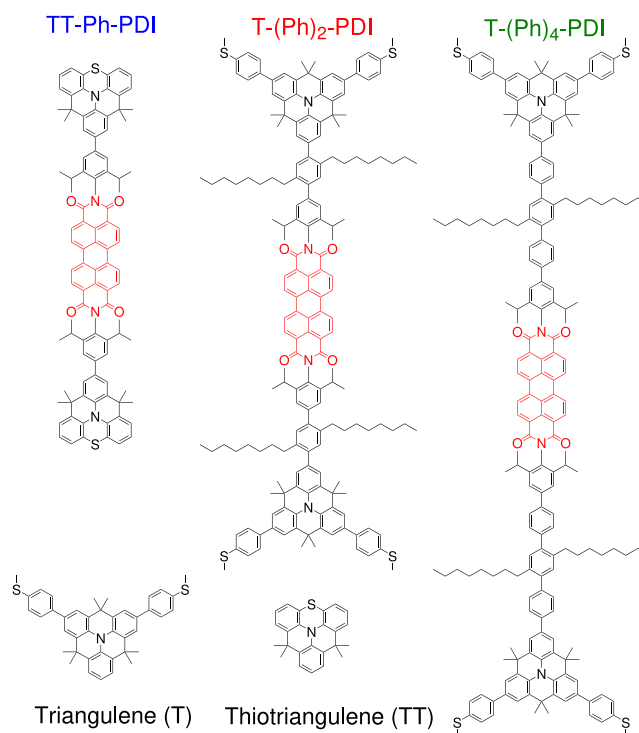
Previous works demonstrate that increasing the donor–acceptor spatial separation slows down charge generation and recombination because of a distance-dependent superexchange charge tunneling mechanism. Furthermore, it has been shown that a transition to a weakly distance-dependent charge transport regime is possible at increased donor–acceptor separation. This mechanism corresponds to a thermally activated charge hopping process between spacer units.<sup>15,16,33–35</sup> Gorczak et al.<sup>36</sup> observed the same distance-dependent behavior for hole transfer, whereas the electron-transfer process was faster and distance-independent. They explained the imbalance of the two processes by differences in delocalization of the initial excitations. Intramolecular ET was also investigated in donor–spacer–acceptor systems and shown to be distance-dependent.<sup>37</sup> Kölle et al.<sup>38</sup> studied CT and ET processes in perylene-diimide (PDI) dyads through polyene spacers with varying length. However, until now, an in-depth study revealing the effect of ET on the efficiency of sequential charge generation has not been presented.

More specifically, with the recent development of non-fullerene acceptors,<sup>39–47</sup> ET competing with CT between the donor and acceptor moieties has to be considered as well.<sup>48,49</sup> Again, molecular D–A systems can be tailored to have both ET and CT, depending on the energetics of the donor and acceptor building blocks, in turn allowing to study both processes in one molecular system.<sup>50–52</sup> A better understanding of the photophysics in a well-controlled D–A multichromophore could help to further fine-tune the efficiency boost brought to the OSC field by nonfullerene acceptors.

Of particular interest in CT systems such as OSCs is the ratio of two rates, the rate of intramolecular generation of a CT state to its nonradiative recombination rate,  $k_{(e^* \rightarrow ct)}/k_{(ct \rightarrow g)}$ . Indeed, in the stationary case and as long as we can neglect electron back-transfer from the CT to the primary excited state and the recombination of the primary excited state itself,  $p_{(e^*)}k_{(e^* \rightarrow ct)} = p_{(ct)}k_{(ct \rightarrow g)}$ , where  $p_{(e^*)}$  is the population of molecules in the primary excited state and  $p_{(ct)}$  is the population of molecules in the CT state. This ratio is effectively a measure of the charge generation efficiency irrespective of the process being an electron transfer, hole transfer, or hole (back)transfer after ET (two-step process). As the internal quantum efficiency is proportional to  $p_{(ct)}/p_{(e^*)}$ , we can improve the total efficiency of the SC by increasing this ratio, for example, by varying the distance between the electron donor and acceptor.

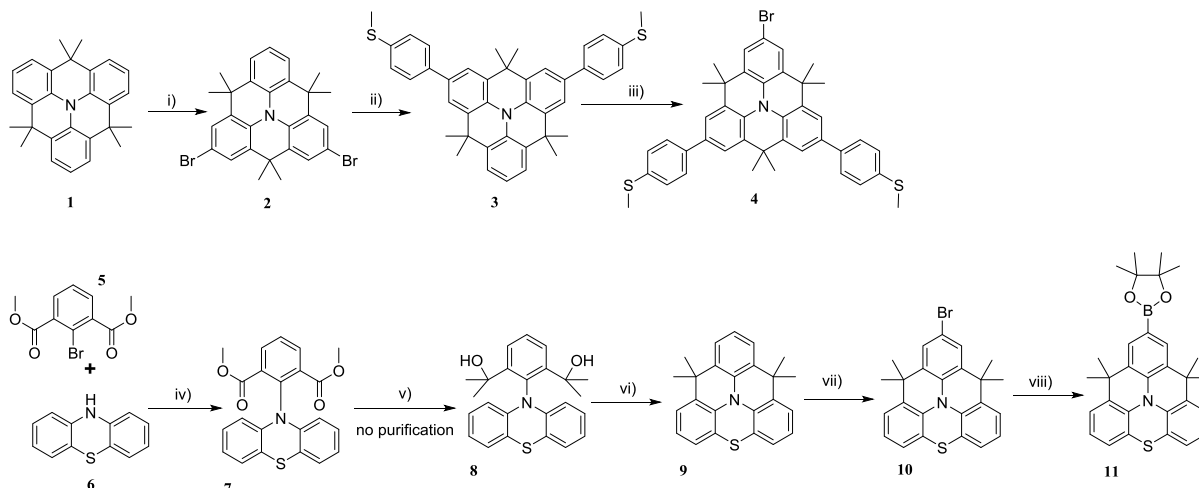
Though both rates are expected to decrease with the spacer length, it is difficult to predict whether their ratio decreases or increases with the length. Furthermore, the rates could be different for direct hole-transfer or sequential energy and hole transfer from the donor to the acceptor, if other electronic or vibronic states are involved. To address these questions, we designed and synthesized a series of symmetric donor–spacer–acceptor–spacer–donor model arrays with different

oligophenylene spacer lengths, varying from one up to four phenylene groups, as depicted in Figure 1. All molecules are

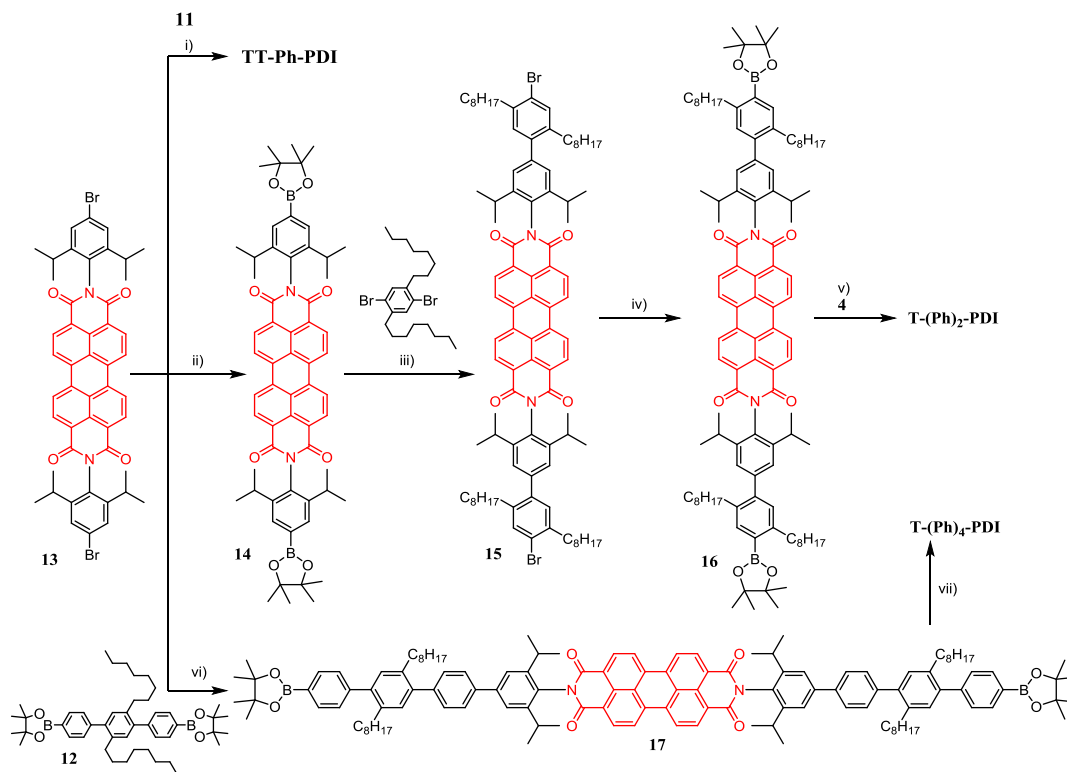


**Figure 1.** Chemical structures of donor–spacer–acceptor–spacer–donor arrays used in this study (TT-Ph-PDI, T-(Ph)<sub>2</sub>-PDI, and T-(Ph)<sub>4</sub>-PDI) as well as two donor moieties (triangulene and thiotriangulene). The PDI core (acceptor) is highlighted in red.

composed of a PDI<sup>53</sup> electron acceptor. In addition to varying the spacer length, the donor strength is altered as well. Precisely, the PDI acceptor is either linked to two triangulene (*N*-heterotriangulene: dimethylmethylene-bridged triphenylamines) or two thiotriangulene (NS-heterotriangulene: dimethylmethylene- and thio-bridged triphenylamines) electron-donating donor moieties. Both triangulene donor units, namely, the *N*-heterotriangulene (T) and NS-heterotriangulene (TT), resemble triphenylamine, a common building block used in organic semiconductors as electron donor and/or charge (hole) transport moiety. We note that the thiotriangulene's reduction potential is about 100 meV higher (closer to the vacuum level) than that of triangulene itself. Compared to triphenylamine, the triangulene (and heterotriangulene) structures are more planar because of the bridging carbon (or sulfur) atoms, in turn allowing closer intermolecular packing and thereby facilitating charge transport. The (thio)-triangulene donor is spatially separated from the electron acceptor PDI by oligophenylene spacers of different lengths: TT-Ph-PDI has one phenylene, while T-(Ph)<sub>2</sub>-PDI and T-(Ph)<sub>4</sub>-PDI employ two and four *para*-oligophenylenes as spacer units, respectively. Although the individual phenylene rings are conjugated, experimentally measured absorption spectra as well as density functional calculations show that the large twisting angle between successive rings interrupts the conjugation between the donor and acceptor units. Using ultrafast transient absorption (TA) spectroscopy, we investigate the effects of increasing spacer length on the generation and recombination rates of intramolecular CT states following photoexcitation of either the acceptor or donor by monitoring

Scheme 1<sup>a</sup>

<sup>a</sup>(i) *N*-Bromosuccinimide, CHCl<sub>3</sub>, 0 °C, 72%; (ii) 1,4-dioxane, K<sub>2</sub>CO<sub>3</sub>, Pd(PPh<sub>3</sub>)<sub>4</sub>, 90 °C, 4 h, 87%; (iii) CHCl<sub>3</sub>/tetrahydrofuran (10:1), NBS, 0 °C, 3 h, 76%; (iv) CuI, Cu, K<sub>2</sub>CO<sub>3</sub>, Ph<sub>2</sub>O, 180 °C, 2 d, 65%; (v) MeMgBr or MeMgI, toluene/Et<sub>2</sub>O, no purification; (vi) H<sub>3</sub>PO<sub>4</sub>, RT, overnight, 43% over two steps; (vii) NBS, CHCl<sub>3</sub>, -10 to 0 °C, 1 h, overnight, 95%; (viii) bis(pinacolato)diboron (B<sub>2</sub>PIN<sub>2</sub>), dimethylformamide, KOAc, Pd(dppf)<sub>2</sub>Cl<sub>2</sub>, 85 °C, 3 h, 68%.

Scheme 2<sup>a</sup>

<sup>a</sup>(i) 12, K<sub>2</sub>CO<sub>3</sub>, Pd(PPh<sub>3</sub>)<sub>4</sub>, toluene/water/EtOH, 85 °C, overnight; 49%; (ii) B<sub>2</sub>PIN<sub>2</sub>, 1,4-dioxane, KOAc, Pd(dppf)<sub>2</sub>Cl<sub>2</sub>, 85 °C, 5 h, 42%; (iii) toluene/water/ethanol, K<sub>2</sub>CO<sub>3</sub>, Pd(PPh<sub>3</sub>)<sub>4</sub>, 85 °C, 8 h, 81%; (iv) B<sub>2</sub>PIN<sub>2</sub>, 1,4-dioxane, KOAc, Pd(dppf)<sub>2</sub>Cl<sub>2</sub>, 85 °C, 12 h, 68%; (v) 4, toluene/water/Aliquat 336, 18-crown-6, K<sub>2</sub>CO<sub>3</sub>, Pd(PPh<sub>3</sub>)<sub>4</sub>, 85 °C, 2 h, 60%; (vi) K<sub>2</sub>CO<sub>3</sub>, Pd(PPh<sub>3</sub>)<sub>4</sub>, toluene/water/EtOH, 85 °C, overnight, 54%; (vii) K<sub>2</sub>CO<sub>3</sub>, Pd(PPh<sub>3</sub>)<sub>4</sub>, toluene/water/Aliquat 336, 85 °C, overnight, 14%.

the spectral evolution of the primary photoexcitation (local exciton) and intramolecular CT states in diluted dichloromethane (DCM) solutions. We apply multivariate curve resolution-alternating least square (MCR-ALS)<sup>54</sup> to separate the component-associated spectra and dynamics of singlet excitons and intramolecular CT states and to accurately

determine the hole- and electron-transfer rates and CT state lifetimes.

## RESULTS AND DISCUSSION

**Synthetic Procedures.** TT-Ph-PDI, T-(Ph)<sub>2</sub>-PDI, and T-(Ph)<sub>4</sub>-PDI were synthesized according to the synthetic

concepts used for rylene-based multichromophores.<sup>55,56</sup> Schemes 1 and 2 depict the three separate steps: synthesis of (1) donor moieties, (2) acceptor units, and (3) coupling of donor and acceptor units.

The functionalized donor subunit, triangulene **4**, was obtained via stoichiometric bisfunctionalization of *N*-heterotriangulene **1** with *N*-bromosuccinimide (NBS). Subsequent Suzuki–Miyaura coupling with 4-(methylthio)phenylboronic acid pinacol ester and an additional NBS bromination yielded the final building block **4** as a colorless powder. The other donor moiety, heterotriangulene **11**, is a newly designed molecule. Its synthesis was based on the synthetic method used for **1**. The inclusion of the sulfur atom into the conjugated backbone of the triarylamine was achieved by utilizing readily available phenothiazine **6** as the starting material. Compound **6** was reacted with dimethyl-2-bromoisophthalate under Ullmann conditions, yielding the diester **7**. Subsequent Grignard reaction and acid-catalyzed intramolecular cyclization afforded the targeted donor building block **9**. Because of the reduced symmetry when comparing **9** and **1**, a selective monobromination could be achieved in the “para”-position with regard to the sulfur atom, yielding **10** with 94%. Subsequent borylation by the Pd-catalyzed reaction led to **11** as a yellow powder.

The synthesis of acceptor units for all three investigated sequences started with dibromo-PDI **13**. Donor building block **11** was directly coupled to **13** via the Suzuki–Miyaura coupling, furnishing **TT-Ph-PDI** in 49%. Incorporation of the solubilizing terphenylene spacer was achieved through a borylation/cross-coupling/borylation cascade reaction using 1,4-dibromo-2,5-dioctylbenzene. The final Suzuki–Miyaura heterocoupling between **16** and triangulene **4** led to the targeted dyad **T-(Ph)<sub>2</sub>-PDI**. In the case of **T-(Ph)<sub>4</sub>-PDI**, the terphenylene spacer **12** was applied, followed by the coupling between **17** and **4**. More detailed synthetic procedures and molecular characterization are provided in Supporting Information Note S1.

**Electronic Properties.** The results of cyclic voltammetry (CV) measurements of multichromophores as well as the neat triangulene donor and PDI acceptor moieties are summarized in Figure 2 (cyclic voltammograms are shown in Supporting Information Note S2). Reduction potentials of the three triads are due to the (thio)triangulene unit. A difference in the reduction potential of about 100 meV between the neat thiotriangulene and triangulene is observed, which translates to a difference of about 50 meV in the title compounds (donor–acceptor triads). The oxidation potential is due to the PDI core and does not change with the spacer length. Density functional theory (DFT) calculations further support this: the highest occupied molecular orbital (HOMO) is localized on the triangulenes/thiotriangulenes, whereas the lowest unoccupied molecular orbital (LUMO) is localized on PDI, as shown in Figure 2 for the compound with the shortest spacer. While CV measurements and DFT calculations confirm the donor–acceptor nature of the molecules, no ground-state CT formation, that is, reduction of perylene diimide/oxidation of (thio)triangulene, is observed in DCM.

**Steady-State Optical Characterization.** UV–vis absorption and steady-state photoluminescence (PL) spectra were recorded in DCM at a concentration of 10<sup>−5</sup> mol/L. As shown in Figure 3, the absorption of the D–A complexes clearly resembles the signatures of its donor and acceptor moieties. The 0–0, 0–1, and 0–2 vibronic bands of PDI can be seen at

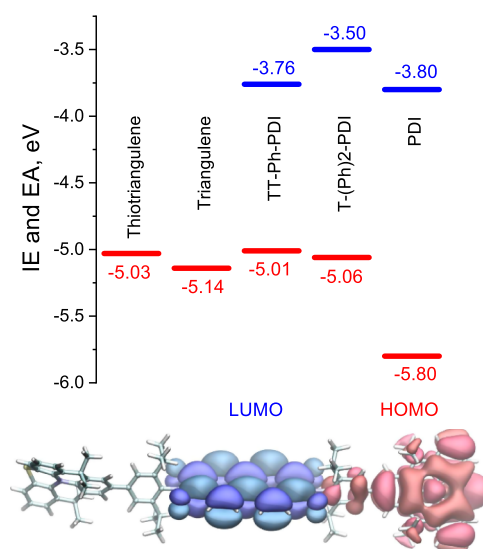


**Figure 2.** Reduction (red) and oxidation (blue) potentials as extracted from CV. Localization of the highest occupied (HOMO, red) and lowest unoccupied (LUMO, blue) orbitals shown for **TT-Ph-PDI** indicates that the conjugation between the donor and acceptor units is indeed broken already for the shortest spacer. Calculations are performed at the m062x/6-31g(d) level of theory using implicit solvent (DCM).

528, 492, and 460 nm, respectively, while the higher energy absorption bands (wavelengths below 400 nm) clearly resemble the absorption of the (thio)triangulene molecules (black lines). However, notable differences also exist between the absorption of different D–A dyads: in **TT-Ph-PDI**, the high energy absorption is red-shifted compared to that of thiotriangulene, while no such shift can be seen in **T-(Ph)<sub>2</sub>-PDI** and **T-(Ph)<sub>4</sub>-PDI**. In addition, the intensity of the first high energy absorption peak at around 370 nm increases with the spacer length. An increase and/or red shift of absorption with spacer length in D–spacer–A-type molecules has been reported previously<sup>37,57,58</sup> and can be explained by the delocalization of the orbitals across the spacer. This is further supported by time-dependent DFT (TD-DFT) calculations: the natural transition orbitals of several lowest energy optical transitions in thiotriangulene, triangulene, **TT-Ph-PDI**, and **T-(Ph)<sub>2</sub>-PDI** are also shown in Figure 3. In all D–A molecules, the first “bright” excited state (denoted as A, state 1 of **TT-Ph-PDI** in Figure 3) corresponds to the first excited state of PDI. The CT state with an electron localized on PDI and a hole on a triangulene has a lower energy (in DCM) but is dark because of the broken conjugation by the spacer between the donor and acceptor blocks. Note that the electronic decoupling of the donor and acceptor is due to a bridging unit with two methyl groups, which lock its orthogonal orientation with respect to the acceptor. Hence, the acceptor is very well decoupled from the bridge and hence from the donor. The entire list of the first 10 excited states, their energies, oscillator strengths, and natural transition orbitals is given in Supporting Information Note S4. The second bright excited state (denoted as B and C in Figure 3) originates from the donor, triangulene. Again, a small red shift with respect to the triangulene itself is due to wavefunction delocalization over the spacer. In the case of **T-(Ph)<sub>2</sub>-PDI** and **T-(Ph)<sub>4</sub>-PDI**, peak C (states 7 and 8, respectively) corresponds to the lowest energy absorption of the triangulene (peak 3, state 1 of triangulene). Peak B of **TT-**

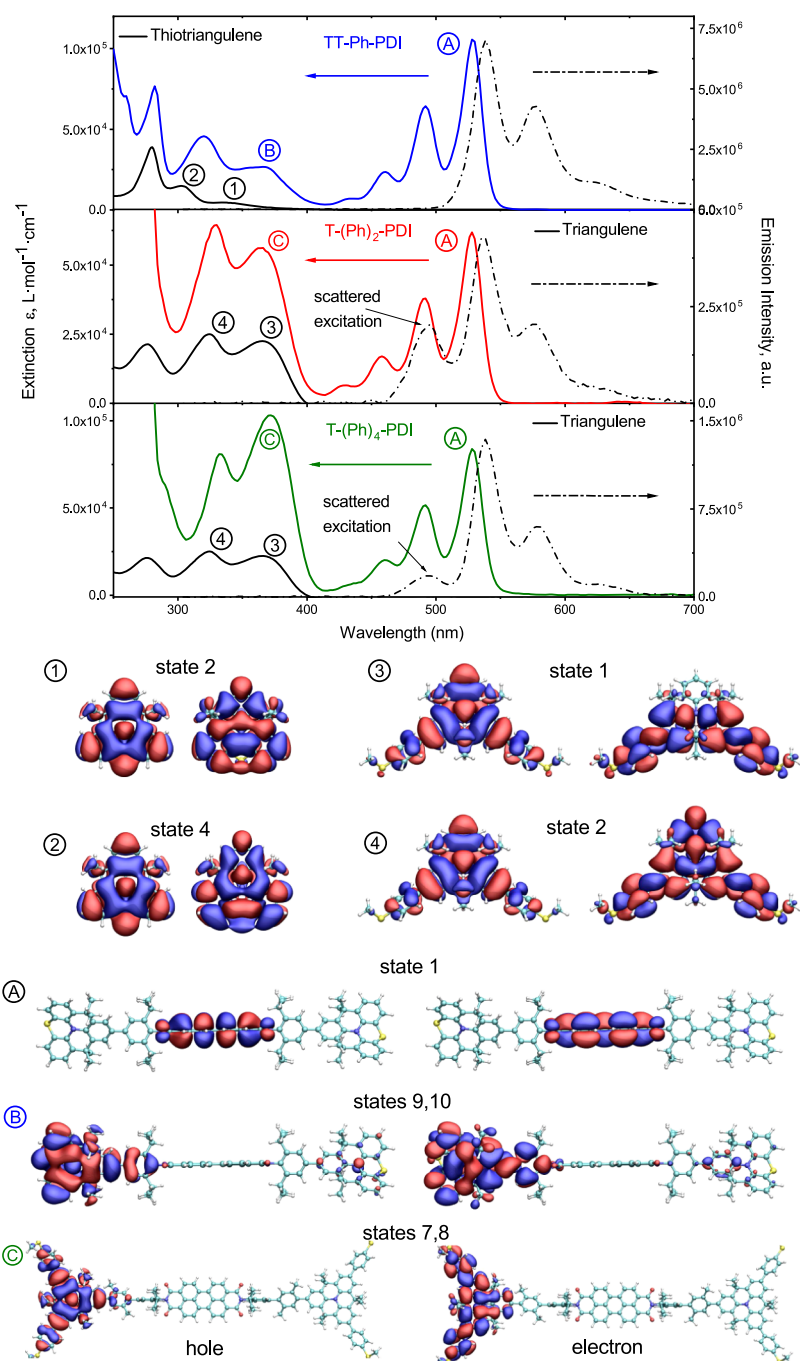


**Figure 3.** UV-vis absorption spectra (solid lines) and fluorescence (dashed-dotted lines) of TT-Ph-PDI (blue) and thiatriangulene, T-(Ph)<sub>2</sub>-PDI (red) and triangulene, and T-(Ph)<sub>4</sub>-PDI (green) and triangulene measured in dilute solutions, together with the natural transition orbitals of TT-Ph-PDI, T-(Ph)<sub>2</sub>-PDI, and the individual triangulene molecules. First 10 orbitals for all compounds are shown in the [Supporting Information](#).

Ph-PDI corresponds to an excited state, which is practically nonabsorbing in thiatriangulene (state 2 is responsible for shoulder 1 of the absorption). In TT-Ph-PDI, this state redshifts and becomes optically active because of the extension over the spacer (state 9 of TT-Ph-PDI). As each D-A dyad has two triangulenes, its molar extinction is doubled in the 300–400 nm spectral region of the D-A dyad. For the same reason, all excited states corresponding to triangulene are doubly degenerate. Overall, none of the 10 lowest energy excited states of the D-A molecules extends over both the PDI and triangulene blocks, indicating a strong decoupling because of the out-of-plane twist of the spacer unit. Such conjugation

breaking,<sup>59–61</sup> together with the alignment of the energy levels of the first optically active and CT states, makes these systems very much alike to donor/acceptor pairs at heterojunction interfaces of OSCs. A clear advantage of D-A-D triads is that the D-A intermolecular distance is (chemically) controlled, greatly simplifying the analysis of the electro-optical processes.

The steady-state fluorescence spectra were measured by exciting the PDI core at 490 nm. The emission spectra, shown in [Figure 3](#) (dashed-dotted line), are similar for all three molecules, mirroring the absorption spectrum of PDI. The fluorescence quantum yields are, however, very low. Because previous studies showed that PDI monomers in solution have a

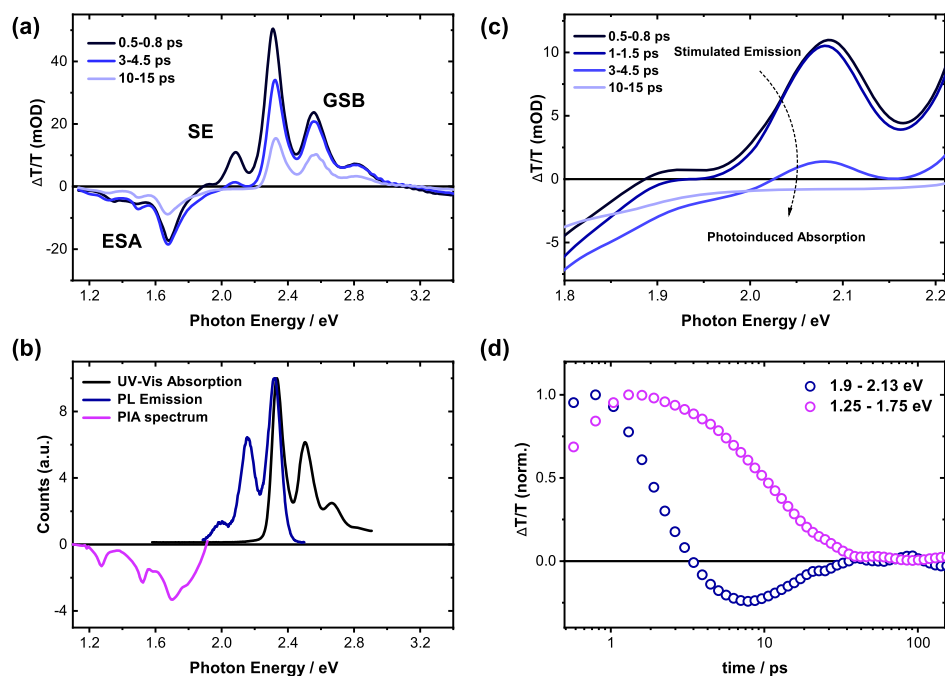


**Figure 4.** (a) TA spectra of TT-Ph-PDI in solution ( $10^{-5}$  mol/L) photoexcited at 490 nm (excitation density  $53 \mu\text{J}/\text{cm}^2$ ). (b) Reconstruction of TA spectra using UV-vis absorption (black line), PL emission (blue line), and PIA spectrum of poly(3-hexylthiophene): PDI (pink line). (c) Spectral evolution from SE to ESA in TT-Ph-PDI. (d) TA kinetics of SE region (integrated between 1.9 and 2.13 eV) and ESA region (integrated between 1.25 and 1.75 eV).

fluorescence quantum yield close to one,<sup>62</sup> we can already anticipate that the PDI excitation is converted to a “dark” state in competition to its fluorescent decay.

**Excited and CT State Dynamics.** To further investigate the fate of the PDI excited state, TA spectra of a dilute solution of TT-Ph-PDI ( $10^{-5}$  mol/L in DCM) were recorded for delay times in the picosecond–nanosecond range after selective excitation of PDI at 490 nm. The TA spectra, shown in Figure 4a, consist of three main features assigned by comparison with independent reference measurements from other spectroscopy techniques, shown in Figure 4b. First, from 2.32 to 3.0 eV, a positive differential transmission signal matching the steady-state UV-vis absorption of PDI (black line) is attributed to the ground-state bleach of the acceptor part of the molecule. Second, between 1.85 and 2.30 eV, a positive TA signal is observed only at early time delays and ties to the PL emission obtained by steady-state PL (blue line) experiments. Thus, these bands are assigned to stimulated emission (SE). Third, below 1.9 eV, a negative signal due to excited-state absorption (ESA) is observed.

The evolution of the TA spectra reveals that a transition occurs between two states. These two states are observed by monitoring the spectral region of SE, shown in Figure 4c. Here, we focus on this spectral region as it shows a clear and fast transition. We first observe the initial SE signal including the 0–1 and 0–2 PDI vibronic peaks of emission from PDI excitons. These peaks decay fast within the first 8 ps and evolve to a broad negative ESA signal, which is significantly longer-lived. The TA kinetics of SE and ESA regions are compared in Figure 4d and clearly show different dynamics. We assign the positive SE signal to the primary photoexcitation, that is, PDI excitons, as the SE signal reflects the population of PDI excitons as seen in Figure 4b. The negative longer-lived ESA signal is assigned to absorption from intramolecular CT states, as the spectral signatures of these long-lived bands match those

of PDI anions. The spectrum of PDI anions, measured by photoinduced absorption (PIA) and presented in Figure 4b, clearly exhibits the same ESA bands at 1.3, 1.5, and 1.68 eV as the ESA observed in TA after a few picoseconds (after the decay of PDI excitons). We therefore conclude that the observed evolution of the TA spectra can be attributed to hole transfer from the photoexcited PDI to the thiotriangulene (see Supporting Information Note S6 for more details about the extraction of the PIA spectrum).

We deconvoluted the TA spectra dynamics into PDI excitons and intramolecular CT states using MCR analysis as explained in Supporting Information Note S7. The component spectra of the MCR analysis match the previously reported spectra of PDI\* (excitons) and PDI anions, supporting that two states are observed.<sup>15,36,63</sup> MCR analysis confirms that we observe two dominating processes upon PDI excitation: hole transfer from the PDI excited state [ $a^*$ ] to the thiotriangulene, forming the charge-transfer [ct] state, and the CT state decay back to the ground state. To extract the CT and charge recombination rates, we used a minimalistic set of rate equations<sup>21,64</sup> for a three-state system, depicted in Figure 5. We omitted back-transfer of the hole from thiotriangulene to PDI because the ionization energy offsets between thiotriangulene and PDI are larger than 0.5 eV that is well above the thermal activation energy.<sup>65</sup> The fluorescence decay of PDI chromophores was also neglected because the PDI fluorescence decay rate in DCM is of the order of  $\sim 2.5 \times 10^8 \text{ s}^{-1}$ ,<sup>62,66</sup> thus well below the sub-100 ps exciton decay predicted by our MCR analysis. To this end, the forward hole-transfer rates and recombination rates of CT states were obtained by applying a global fit on the MCR output dynamics using the solution of the rate equations as explained in Supporting Information Note S9.

Figure 6 shows the experimentally determined population dynamics of PDI excitons and CT states in all three model

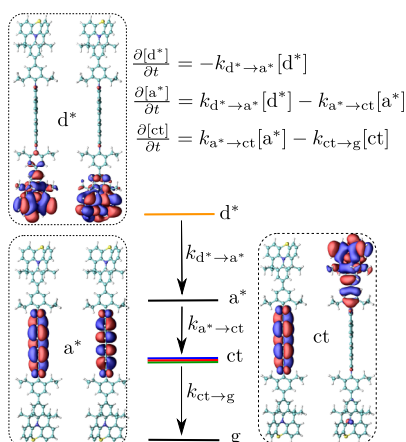


**Figure 5.** Four-state model used to fit the experimental data.  $k_{a^* \rightarrow g}$  and  $k_{ct \rightarrow g}$  are the decay rates of excited singlet and CT states to the ground state,  $k_{a^* \rightarrow ct}$  is the hole-transfer rate from the PDI to the triangulene block, and  $k_{d^* \rightarrow a^*}$  is the ET rate from the donor to the acceptor (PDI) and is only present if the donor is excited.

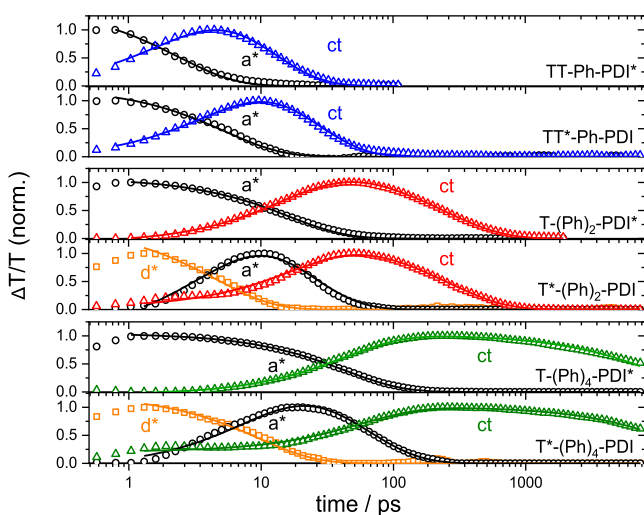


**Figure 6.** Population of PDI excitons (black circles), triangulene excitons (orange rectangles), and intramolecular CT states (blue triangles for TT-Ph-PDI, red triangles for T-(Ph)<sub>2</sub>-PDI, and green triangles for T-(Ph)<sub>4</sub>-PDI) upon acceptor excitation (D–S–A\*) and upon donor excitation (D\*–S–A). Dynamics of thiotriangulene excitons in TT\*-Ph-PDI are not shown because their decay is much faster than the temporal resolution of our TA setup. Global fits of equations explained in Supporting Information Note S9 are shown as solid lines. The observed initial rise of the CT state population is due to the excitation laser pulse.

triads, together with their fits. The CT state generation and recombination rates, as well as their ratios, are summarized in Table 1. In OSCs, donor and acceptor absorption spectra can complement each other, thereby helping to harvest a larger part of the solar spectrum. To gain more insights into the role of the donor excitation on the processes occurring at the D–A interface, we also performed TA measurements following excitation of the donor at 355 nm. Analysis of the TA spectra presented in Supporting Information Note S8 clearly indicates that an additional process takes place upon donor excitation and can be assigned to the ET from the excited donor to the PDI core.<sup>67</sup> To extract the CT and charge recombination rates, we additionally took into account the ET process, as illustrated in Figure 5. The corresponding fit of the output of the MCR

**Table 1.** Energy Transfer, Generation, and Recombination Rates of Intramolecular CT States Determined by Fitting the Population Dynamics of MCR Outputs<sup>a</sup>

excitation	energy transfer $k_{d^* \rightarrow a^*}$ [ $\times 10^9$ s <sup>-1</sup> ]	generation $k_{a^* \rightarrow ct}$ [ $\times 10^9$ s <sup>-1</sup> ]	recombination $k_{ct \rightarrow g}$ [ $\times 10^9$ s <sup>-1</sup> ]	$k_{a^* \rightarrow ct}/k_{ct \rightarrow g}$
TT-Ph-PDI*		416 ± 12	99 ± 3	4.2
T-(Ph) <sub>2</sub> -PDI*		62 ± 0.6	4.0 ± 0.04	15.5
T-(Ph) <sub>4</sub> -PDI*		23 ± 0.2	0.11 ± 0.001	209.1
TT*-Ph-PDI	>10 000	187 ± 4	47 ± 1.1	4.0
T*(Ph) <sub>2</sub> -PDI	217 ± 5	50.3 ± 1	3.8 ± 0.07	13.2
T*(Ph) <sub>4</sub> -PDI	105 ± 2	17.3 ± 0.3	0.07 ± 0.003	247.1

<sup>a</sup>D–S–A\* solutions were photoexcited at 490 nm. D\*–S–A solutions were photoexcited at 355 nm. Energy transfer, charge generation, and recombination rates are extracted by fitting the population dynamics of MCR outputs.

analysis is shown in Figure 6. The rates of energy and hole transfer as well as charge recombination are summarized in Table 1. As expected, the ET rate from T\*(Ph)<sub>4</sub>-PDI to T-(Ph)<sub>4</sub>-PDI\* is smaller than that from T\*(Ph)<sub>2</sub>-PDI to T-(Ph)<sub>2</sub>-PDI\* because the donor and acceptor are further apart in T-(Ph)<sub>4</sub>-PDI. However, the ratio of the rates does not obey the Förster rate expression,  $k \approx d^{-6}$ , because the donor and the acceptor are too close to each other to justify the dipole–dipole interaction approximation (this would theoretically amount to a ratio of  $\sim(27/19)^6 \approx 6$  as compared to 217/105  $\approx 2$  observed experimentally). The ultrafast ET in TT-Ph-PDI is a first indication that in this multichromophore triad Dexter-type ET takes place. This conclusion is further supported by DFT calculations, which demonstrate that the donor orbitals are partially delocalized over the spacer unit closest to them, resulting in a partial direct overlap between the donor and acceptor orbitals participating in the ET reaction.

## DISCUSSION

Several remarkable observations can be made by comparing the dynamics of CT state formation and recombination upon donor and acceptor excitation of the triads studied here. When the donor is excited, the population of CT states in TT-Ph-PDI reaches its maximum at around 10 ps and decays to zero at around 200 ps. When the acceptor is excited, these values are much smaller, ca 5 and 50 ps, respectively, resulting in much higher CT state generation and recombination rates in TT-Ph-PDI\* as compared to that in TT\*-Ph-PDI. This is surprising: in all three multichromophores fast ET takes place, effectively converting D\*–S–A into D–S–A\* prior to the CT state formation and recombination. In fact, in T-(Ph)<sub>2</sub>-PDI and T-(Ph)<sub>4</sub>-PDI, the CT state formation and recombination rates are practically unaffected by the type of the initial excitations. We excluded degradation by UV (355 nm) laser exposure as a reason for varying rates in TT\*-Ph-PDI compared to that in TT-Ph-PDI\* by remeasuring the same sample with 490 nm excitation (Figure S14) after UV exposure. Hence, the only remaining explanation of this observation is that the energy of the first excited state of the donor (thiotriangulene, TT) is comparable (slightly above, see Supporting Information Note S4) to the second excited state of the acceptor (PDI). The second excited state of PDI is, however, a dark state. Consequently, Förster-type ET to this state is not possible but, because of the short spacer of TT-Ph-PDI, Dexter-type ET to the second excited state can still take

place. An immediate implication is that the second CT state can be populated and recombine to the ground state, however, now with different generation and recombination rates compared to those observed after the direct excitation of PDI. This can potentially impact the performance of OPV devices, where exciton conversion into a higher-lying CT state can boost the subsequent transition of the CT to charge-separated states and needs to be considered in donor–acceptor systems, in which one or both of the components have higher-lying dark states. However, the ratio of charge generation/recombination rates for both TT-Ph-PDI\* and TT\*-Ph-PDI excitation is the same (see Table 1), implying that populating higher-lying dark states does not affect the charge generation efficiency. We note that PDI is an often-used building block in the design of novel nonfullerene acceptors, thus similar phenomena may occur in OPV blends that use materials based on PDIs.

To rationalize the dependence of the rates on the spacer length, we employ the Marcus expression for the CT rate

$$k_{\text{CT}} = \frac{2\pi}{h\sqrt{4\pi\lambda k_{\text{B}}T}} J^2 \exp\left[-\frac{(\lambda + \Delta G)^2}{4\lambda k_{\text{B}}T}\right]$$

where  $\Delta G$  is the driving force or the free energy difference between the states,  $J$  is the electronic coupling element, and  $\lambda$  is the reorganization energy. For TT-Ph-PDI, for example, the calculations predict for the CT to ground-state transition a driving force of  $\Delta G_{\text{ct}\rightarrow\text{g}} = 1.04$  eV and a reorganization energy  $\lambda_{\text{ct}\rightarrow\text{g}} = 1.03$  eV. For the  $\text{a}^*$  to CT state transition, we obtain  $\Delta G_{\text{a}^*\rightarrow\text{ct}} = 0.003$  eV,  $\lambda_{\text{a}^*\rightarrow\text{ct}} = 0.063$  eV. Correspondingly, the ratio of Boltzmann prefactors in the rate is 0.54, indicating that the ratio of the HOMO/HOMO to HOMO/LUMO electronic coupling is of the order of 10 because the experimentally measured rate ratio for TT-Ph-PDI is  $\sim 4.2$ .

The calculations show that the driving force for the excited ( $\text{a}^*$ ) to CT state slightly increases with the spacer length and so does the reorganization energy. The overall reaction barrier,  $(\lambda + \Delta G)^2/4\lambda$ , slightly decreases. We can therefore conclude that the main reason for the decrease of the CT state generation rate, given in Table 1 and displayed in Figure 7, is the decrease of the electronic coupling between the donor and acceptor units. For the CT to the ground-state reaction, the driving force decreases and reorganization energy increases with the spacer length. Hence, the CT state recombination slow-down is affected by both the increasing barrier and decreasing electronic coupling. This explains an exponential increase of the ratio of the generation and recombination rates, which is presented in the inset of Figure 7.

## CONCLUSIONS

The photophysical studies of donor–spacer–acceptor–spacer–donor systems offer important implications for donor–acceptor heterojunction interfaces and OPVs in general. First, a controversial conclusion is that a longer spacer between the donor and acceptor blocks is beneficial for populating CT states, in spite of the slowing down of the CT state generation. This effect can be used in a bulk heterojunction cell. Indeed, more efficient molecular CT state generation as compared to recombination reduces overall geminate recombination in a PV device.<sup>68</sup> In addition, larger donor–acceptor separations lead to smaller Coulomb binding energies of CT states and hence facilitate formation of charge-separated states from CT states, enabling CT state splitting

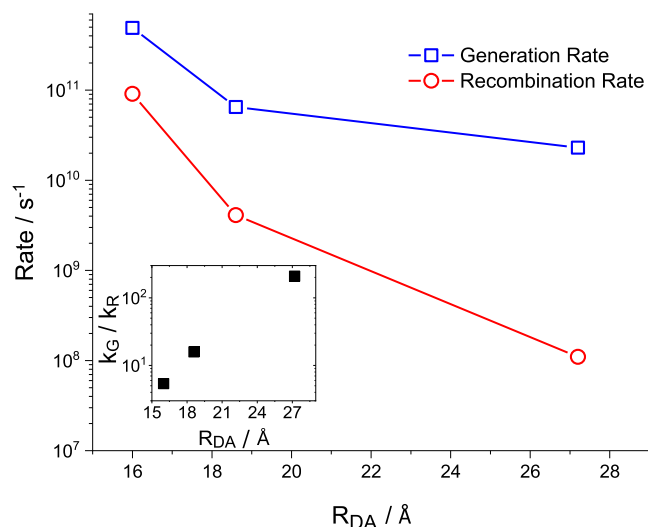


**Figure 7.** Semilogarithmic plot of the charge generation rate (blue squares) and charge recombination rate (red circles) as a function of the donor–acceptor distance. Centers of mass of the corresponding units are used to quantify their separations. Inset: Semilogarithmic plot of the ratio of the generation rate,  $k_{\text{G}}$ , and the recombination rate  $k_{\text{R}}$ , as a function of the donor–acceptor distance.

even in a single-component OSC, as reported recently.<sup>69,70</sup> Chemically, this can be realized by shielding groups participating in the CT state formation. Care, however, should be taken because steric shielding might also reduce charge mobility in pristine mesophases.

Second, ET between the donor and acceptor can take place, if the donor emission and the acceptor absorption spectra overlap or spatial separations between the donor and acceptor are small. For bulk heterojunction OPV, ET provides an additional degree of freedom in designing the energy level offsets. Indeed, efficient splitting of an excited state requires sizable offsets between ionization energies (acceptor excitation) or electron affinities (donor excitation). If efficient ET takes place, say from the donor to the acceptor, then the only requirement is to have a large offset of the ionization energy because the acceptor is solely responsible for splitting the excited states.

Third, it appears that the short-range Dexter-type ET can involve higher excited (and, consequently, CT) states, if the spectra of the donor and acceptor are complementary. The higher-lying excited states are “dark” states, which contribute to CT state formation. In fact, this concept could be explored in novel donor–acceptor systems and used to our advantage because energetically higher CT states can provide larger driving forces for the CT to charge-separated state reactions and hence reduce both geminate and nongeminate recombination.

## EXPERIMENTAL METHODS

**TA Spectroscopy.** TA spectroscopy was carried out using a homebuilt pump–probe setup. Two different configurations of the setup were used for either short delay, namely, 100 fs to 8 ns experiments, or long delay, namely, 1 ns to 100  $\mu\text{s}$  delays, as described below: the output of a titanium:sapphire amplifier (Coherent Legend Duo, 4.5 mJ, 3 kHz, 100 fs) was split into three beams (2, 1, and 1.5 mJ). Two of them were used to separately pump two optical parametric amplifiers (Light Conversion TOPAS Prime). TOPAS 1 generates tunable 490

nm in addition to 710 pump pulses, subsequently frequency doubled to 355 nm with a 2 mm thick barium metaborate (BBO) crystal, whereas TOPAS 2 generates signal (1300 nm) and idler (2000 nm) only. For measuring TA in the visible range, we used 1300 nm (signal) of TOPAS 2 to produce white-light super continuum from 350 to 1100 nm in a calcium fluoride ( $\text{CaF}_2$ ) window. For short delay TA measurements, TOPAS 1 was used to generate pump pulses, while the probe pathway length to the sample was kept constant at  $\approx 5$  m between the output of TOPAS 1 and the sample. The pump pathway length was varied between 5.12 and 2.6 m with a broadband retroreflector mounted on an automated mechanical delay stage (Newport linear stage IMS600CCHA controlled by a Newport XPS motion controller), thereby generating delays between pump and probe from  $-400$  ps to 8 ns. For the 1 ns to 300  $\mu\text{s}$  delay (long delay) TA measurement, the same probe white-light supercontinuum was used as for the 100 fs to 8 ns delays. Here, the excitation light (pump pulse) was provided by an actively Q-switched Nd:YVO<sub>4</sub> laser (InnoLas piccolo AOT) frequency-doubled to provide pulses at 532 nm. The pump laser was triggered by an electronic delay generator (Stanford Research Systems DG535), itself triggered by the transistor–transistor logic sync from the Legend Duo, allowing control of the delay between pump and probe with a jitter of roughly 100 ps. Pump and probe beams were focused on the sample which was kept under a dynamic vacuum of  $<10$ –5 mbar. The transmitted fraction of the white light was guided to a custom-made prism spectrograph (Entwicklungsbüro Stresing) where it was dispersed by a prism onto a 512 pixel negative channel metal–oxide–semiconductor linear image sensor (Hamamatsu S8381-512) and a 512 pixel complementary metal–oxide–semiconductor linear image sensor (Hamamatsu G11608-512DA). The probe pulse repetition rate was 3 kHz, while the excitation pulses were mechanically chopped to 1.5 kHz (100 fs to 8 ns delays) or directly generated at 1.5 kHz frequency (1 ns to 300  $\mu\text{s}$  delays), while the detector array was read out at 3 kHz. Adjacent diode readings corresponding to the transmission of the sample after excitation and in the absence of an excitation pulse were used to calculate  $\Delta T/T$ . Measurements were averaged over several thousand shots to obtain a good signal-to-noise ratio.

**MCR-ALS Analysis.** To separate the TA spectra and determine the spectral weight of each component, MCR-ALS analysis<sup>71,72</sup> was applied to an augmented matrix composed of TA data at different excitation fluences. Singular value decomposition was applied to estimate the number of components present in the data matrix. One constraint was applied to the analysis that is non-negativity of concentration.

**Theoretical Calculations.** Ground-state geometries were optimized using the m062x range-separated functional and the 6-311g(d) basis set. All optimizations were performed in the implicit solvent (DCM) using the IEFPCM model. Absorption spectra were calculated at the same level of theory using the nonequilibrium solvation model (PISALR) in which only the electronic relaxation is taken into account. All calculations were performed using the GAUSSIAN 09 package.

Averaged vertical excitation energies were calculated using the m062x range-separated functional and the 6-311g(d) basis set. Polarizable continuum model (PCM)<sup>73–75</sup> was used to account for the solvent stabilization. All calculations were performed using the GAUSSIAN09 package.

To evaluate (ensemble-averaged) vertical excitation energies, we used the PCM.<sup>73–75</sup> We first performed geometry optimizations in the g, ct, and a\* states at the m062x/6-31g(d) level of theory using DCM as an implicit solvent, saved the optimized solvent state, and then evaluated the excited-state energies of other states in the saved (nonequilibrium) solvation shells.

Driving forces and reorganization energies were calculated using the m062x range-separated functional and the 6-311g(d) basis set and are summarized in Supporting Information Note S10. PCM<sup>73–75</sup> was used to account for the solvent stabilization. All calculations were performed using the GAUSSIAN09 package.<sup>76</sup>

## ■ ASSOCIATED CONTENT

### 📄 Supporting Information

The Supporting Information is available free of charge on the ACS Publications website at DOI: 10.1021/acs.jpcc.9b05149.

Details of synthesis, CV, UV–vis spectrum, TD-DFT calculation details, MCR-ALS analysis, and TA spectra (PDF)

## ■ AUTHOR INFORMATION

### Corresponding Authors

\*E-mail: muellen@mpip-mainz.mpg.de (K.M.).

\*E-mail: denis.andrienko@mpip-mainz.mpg.de (D.A.).

\*E-mail: frederic.laquai@kaust.edu.sa (F.L.).

### ORCID

Klaus Müllen: 0000-0001-6630-8786

Denis Andrienko: 0000-0002-1541-1377

Frédéric Laquai: 0000-0002-5887-6158

### Present Address

<sup>§</sup>School of Environment and Civil Engineering, Dongguan University of Technology, No. 1, Daxue Rd., Songshan Lake, Dongguan, Guangdong Province, P. R. China.

### Author Contributions

<sup>||</sup>A.H.B and S.S contributed equally.

### Notes

The authors declare no competing financial interest.

## ■ ACKNOWLEDGMENTS

This publication is based upon work supported by the King Abdullah University of Science and Technology (KAUST) Office of Sponsored Research (OSR) under Award No: OSR-2018-CARF/CCF-3079. D.A. received funding from the BMBF grant InterPhase and MESOMERIE (FKZ 13N13661, FKZ 13N13656) and the European Union Horizon 2020 research and innovation program “Widening materials models” under grant agreement no. 646259 (MOSTOPHOS). D.A. also acknowledges KAUST and the PSE division for hosting his sabbatical in the framework of the Visiting Faculty Program.

## ■ REFERENCES

- (1) Polívka, T.; Sundström, V. Ultrafast Dynamics of Carotenoid Excited States—From Solution to Natural and Artificial Systems. *Chem. Rev.* **2004**, *104*, 2021–2072.
- (2) Blankenship, R. E. *Molecular Mechanisms of Photosynthesis*; John Wiley & Sons, 2013.
- (3) Mirkovic, T.; Ostroumov, E. E.; Anna, J. M.; van Grondelle, R.; Govindjee, G. D.; Scholes, G. D. Light Absorption and Energy

Transfer in the Antenna Complexes of Photosynthetic Organisms. *Chem. Rev.* **2016**, *117*, 249–293.

(4) Kudo, A.; Miseki, Y. Heterogeneous Photocatalyst Materials for Water Splitting. *Chem. Soc. Rev.* **2009**, *38*, 253–278.

(5) Li, Q.; Guo, B.; Yu, J.; Ran, J.; Zhang, B.; Yan, H.; Gong, J. R. Highly Efficient Visible-Light-Driven Photocatalytic Hydrogen Production of Cds-Cluster-Decorated Graphene Nanosheets. *J. Am. Chem. Soc.* **2011**, *133*, 10878–10884.

(6) Ingram, G. L.; Nguyen, C.; Lu, Z.-H. Long-Range Energy Transfer and Singlet-Exciton Migration in Working Organic Light-Emitting Diodes. *Phys. Rev. Appl.* **2016**, *5*, 064002.

(7) Heimel, P.; Mondal, A.; May, F.; Kowalsky, W.; Lennartz, C.; Andrienko, D.; Lovrincic, R. Unicolored Phosphor-Sensitized Fluorescence for Efficient and Stable Blue Oleds. *Nat. Commun.* **2018**, *9*, 4990.

(8) Menke, S. M.; Holmes, R. J. Exciton Diffusion in Organic Photovoltaic Cells. *Energy Environ. Sci.* **2014**, *7*, 499–512.

(9) Lyons, B. P.; Clarke, N.; Groves, C. The Relative Importance of Domain Size, Domain Purity and Domain Interfaces to the Performance of Bulk-Heterojunction Organic Photovoltaics. *Energy Environ. Sci.* **2012**, *5*, 7657–7663.

(10) Li, Z.; Xu, X.; Zhang, W.; Meng, X.; Ma, W.; Yartsev, A.; Inganäs, O.; Andersson, M. R.; Janssen, R. A. J.; Wang, E. High Performance All-Polymer Solar Cells by Synergistic Effects of Fine-Tuned Crystallinity and Solvent Annealing. *J. Am. Chem. Soc.* **2016**, *138*, 10935–10944.

(11) Ye, L.; Jiao, X.; Zhao, W.; Zhang, S.; Yao, H.; Li, S.; Ade, H.; Hou, J. Manipulation of Domain Purity and Orientational Ordering in High Performance All-Polymer Solar Cells. *Chem. Mater.* **2016**, *28*, 6178–6185.

(12) Kumar, P.; Shivananda, K. N.; Zajączkowski, W.; Pisula, W.; Eichen, Y.; Tessler, N. The Relation between Molecular Packing or Morphology and Chemical Structure or Processing Conditions: The Effect on Electronic Properties. *Adv. Funct. Mater.* **2014**, *24*, 2530–2536.

(13) Laquai, F.; Andrienko, D.; Deibel, C.; Neher, D. Charge Carrier Generation, Recombination, and Extraction in Polymer–Fullerene Bulk Heterojunction Organic Solar Cells. *Elementary Processes in Organic Photovoltaics*; Springer, 2017; pp 267–291.

(14) Poelking, C.; Andrienko, D. Design Rules for Organic Donor-Acceptor Heterojunctions: Pathway for Charge Splitting and Detrapping. *J. Am. Chem. Soc.* **2015**, *137*, 6320–6326.

(15) Weiss, E. A.; Ahrens, M. J.; Sinks, L. E.; Gusev, A. V.; Ratner, M. A.; Wasielewski, M. R. Making a Molecular Wire: Charge and Spin Transport through para-Phenylene Oligomers. *J. Am. Chem. Soc.* **2004**, *126*, 5577–5584.

(16) Davis, W. B.; Svec, W. A.; Ratner, M. A.; Wasielewski, M. R. Molecular-wire behaviour in p-phenylenevinylene oligomers. *Nature* **1998**, *396*, 60.

(17) Howard, I. A.; Meister, M.; Baumeier, B.; Wonneberger, H.; Pschirer, N.; Sens, R.; Bruder, I.; Li, C.; Müllen, K.; Andrienko, D.; Laquai, F. Two Channels of Charge Generation in Perylene Monoimide Solid-State Dye-Sensitized Solar Cells. *Adv. Energy Mater.* **2014**, *4*, 1300640.

(18) Hörmann, U.; Zeiske, S.; Piersimoni, F.; Hoffmann, L.; Schlesinger, R.; Koch, N.; Riedl, T.; Andrienko, D.; Neher, D. Stark Effect of Hybrid Charge Transfer States at Planar ZnO/Organic Interfaces. *Phys. Rev. B* **2018**, *98*, 155312.

(19) Meister, M.; Baumeier, B.; Pschirer, N.; Sens, R.; Bruder, I.; Laquai, F.; Andrienko, D.; Howard, I. A. Observing Charge Dynamics in Surface Reactions by Time-Resolved Stark Effects. *J. Phys. Chem. C* **2013**, *117*, 9171–9177.

(20) Shoer, L. E.; Eaton, S. W.; Margulies, E. A.; Wasielewski, M. R. Photoinduced Electron Transfer in 2,5,8,11-Tetrakis-Donor-Substituted Perylene-3,4:9,10-bis(dicarboximides). *J. Phys. Chem. B* **2014**, *119*, 7635–7643.

(21) Petrozza, A.; Laquai, F.; Howard, I. A.; Kim, J.-S.; Friend, R. H. Dielectric Switching of the Nature of Excited Singlet State in a Donor-

Acceptor-Type Polyfluorene Copolymer. *Phys. Rev. B: Condens. Matter Mater. Phys.* **2010**, *81*, 205421.

(22) Hinkel, F.; Kim, Y. M.; Zagariarsky, Y.; Schlütter, F.; Andrienko, D.; Müllen, K.; Laquai, F. Efficiency-Limiting Processes in Cyclopentadithiophene-Bridged Donor-Acceptor-Type Dyes for Solid-State Dye-Sensitized Solar Cells. *J. Chem. Phys.* **2018**, *148*, 044703.

(23) Wiebeler, C.; Plasser, F.; Hedley, G. J.; Ruseckas, A.; Samuel, I. D. W.; Schumacher, S. Ultrafast Electronic Energy Transfer in an Orthogonal Molecular Dyad. *J. Phys. Chem. Lett.* **2017**, *8*, 1086–1092.

(24) Scholes, G. D. Long-Range Resonance Energy Transfer in Molecular Systems. *Annu. Rev. Phys. Chem.* **2003**, *54*, 57–87.

(25) Ishizaki, A.; Fleming, G. R. Unified Treatment of Quantum Coherent and Incoherent Hopping Dynamics in Electronic Energy Transfer: Reduced Hierarchy Equation Approach. *J. Chem. Phys.* **2009**, *130*, 234111.

(26) Marcus, R. A.; Sutin, N. Electron Transfers in Chemistry and Biology. *Biochim. Biophys. Acta, Bioenerg.* **1985**, *811*, 265–322.

(27) Ivanov, A. I.; Dereka, B.; Vauthey, E. A Simple Model of Solvent-Induced Symmetry-Breaking Charge Transfer in Excited Quadrupolar Molecules. *J. Chem. Phys.* **2017**, *146*, 164306.

(28) Dereka, B.; Rosspeintner, A.; Li, Z.; Liska, R.; Vauthey, E. Direct Visualization of Excited-State Symmetry Breaking Using Ultrafast Time-Resolved Infrared Spectroscopy. *J. Am. Chem. Soc.* **2016**, *138*, 4643–4649.

(29) Segura, J. L.; Martín, N.; Guldi, D. M. Materials for Organic Solar Cells: The C 60/PI-Conjugated Oligomer Approach. *Chem. Soc. Rev.* **2005**, *34*, 31–47.

(30) Roncali, J. Linear  $\Pi$ -Conjugated Systems Derivatized with C 60-Fullerene as Molecular Heterojunctions for Organic Photovoltaics. *Chem. Soc. Rev.* **2005**, *34*, 483–495.

(31) Wang, M.; Wudl, F. Top-Down Meets Bottom-Up: Organized Donor–Acceptor Heterojunctions for Organic Solar Cells. *J. Mater. Chem.* **2012**, *22*, 24297–24314.

(32) Figueira-Duarte, T. M.; Gégout, A.; Nierengarten, J.-F. Molecular and Supramolecular C 60–Oligophenylenevinylene Conjugates. *Chem. Commun.* **2007**, 109–119.

(33) Malak, R. A.; Gao, Z.; Wishart, J. F.; Isied, S. S. Long-Range Electron Transfer across Peptide Bridges: The Transition from Electron Superexchange to Hopping. *J. Am. Chem. Soc.* **2004**, *126*, 13888–13889.

(34) Lewis, F. D.; Zhu, H.; Daublain, P.; Fiebig, T.; Raytchev, M.; Wang, Q.; Shafirovich, V. Crossover from Superexchange to Hopping as the Mechanism for Photoinduced Charge Transfer in DNA Hairpin Conjugates. *J. Am. Chem. Soc.* **2006**, *128*, 791–800.

(35) Jiang, J.; Alsam, A.; Wang, S.; Aly, S. M.; Pan, Z.; Mohammed, O. F.; Schanze, K. S. Effect of Conjugation Length on Photoinduced Charge Transfer in  $\pi$ -Conjugated Oligomer-Acceptor Dyads. *J. Phys. Chem. A* **2017**, *121*, 4891–4901.

(36) Gorczak, N.; Tarkuç, S.; Renaud, N.; Houtepen, A. J.; Eelkema, R.; Siebbeles, L. D. A.; Grozema, F. C. Different Mechanisms for Hole and Electron Transfer Along Identical Molecular Bridges: The Importance of the Initial State Delocalization. *J. Phys. Chem. A* **2014**, *118*, 3891–3898.

(37) Harriman, A.; Mallon, L. J.; Elliot, K. J.; Haelele, A.; Ulrich, G.; Ziessel, R. Length Dependence for Intramolecular Energy Transfer in Three- and Four-Color Donor–Spacer–Acceptor Arrays. *J. Am. Chem. Soc.* **2009**, *131*, 13375–13386.

(38) Kölle, P.; Pugliesi, I.; Langhals, H.; Wilcken, R.; Esterbauer, A. J.; de Vivie-Riedle, R.; Riedle, E. Hole-transfer induced energy transfer in perylene diimide dyads with a donor-spacer-acceptor motif. *Phys. Chem. Chem. Phys.* **2015**, *17*, 25061–25072.

(39) Alamoudi, M. A.; Khan, J. I.; Firdaus, Y.; Wang, K.; Andrienko, D.; Beaujuge, P. M.; Laquai, F. Impact of Nonfullerene Acceptor Core Structure on the Photophysics and Efficiency of Polymer Solar Cells. *ACS Energy Lett.* **2018**, *3*, 802–811.

(40) Baran, D.; Gasparini, N.; Wadsworth, A.; Tan, C. H.; Wehbe, N.; Song, X.; Hamid, Z.; Zhang, W.; Neophytou, M.; Kirchartz, T. Robust Nonfullerene Solar Cells Approaching Unity External

Quantum Efficiency Enabled by Suppression of Geminate Recombination. *Nat. Commun.* **2018**, *9*, 2059.

(41) Wadsworth, A.; Moser, M.; Marks, A.; Little, M. S.; Gasparini, N.; Brabec, C. J.; Baran, D.; McCulloch, I. Critical Review of the Molecular Design Progress in Non-Fullerene Electron Acceptors Towards Commercially Viable Organic Solar Cells. *Chem. Soc. Rev.* **2019**, *48*, 1596–1625.

(42) Cheng, P.; Wang, J.; Zhang, Q.; Huang, W.; Zhu, J.; Wang, R.; Chang, S.-Y.; Sun, P.; Meng, L.; Zhao, H.; Cheng, H.-W.; Huang, T.; Liu, Y.; Wang, C.; Zhu, C.; You, W.; Zhan, X.; Yang, Y. Unique Energy Alignments of a Ternary Material System toward High-Performance Organic Photovoltaics. *Adv. Mater.* **2018**, *30*, 1801501.

(43) Kan, B.; Zhang, J.; Liu, F.; Wan, X.; Li, C.; Ke, X.; Wang, Y.; Feng, H.; Zhang, Y.; Long, G. Fine-Tuning the Energy Levels of a Nonfullerene Small-Molecule Acceptor to Achieve a High Short-Circuit Current and a Power Conversion Efficiency over 12% in Organic Solar Cells. *Adv. Mater.* **2018**, *30*, 1704904.

(44) Nian, L.; Kan, Y.; Wang, H.; Gao, K.; Xu, B.; Rong, Q.; Wang, R.; Wang, J.; Liu, F.; Chen, J. Ternary Non-Fullerene Polymer Solar Cells with 13.51% Efficiency and a Record-High Fill Factor of 78.13%. *Energy Environ. Sci.* **2018**, *11*, 3392–3399.

(45) Song, X.; Gasparini, N.; Ye, L.; Yao, H.; Hou, J.; Ade, H.; Baran, D. Controlling Blend Morphology for Ultrahigh Current Density in Nonfullerene Acceptor-Based Organic Solar Cells. *ACS Energy Lett.* **2018**, *3*, 669–676.

(46) Sun, C.; Pan, F.; Bin, H.; Zhang, J.; Xue, L.; Qiu, B.; Wei, Z.; Zhang, Z.-G.; Li, Y. A Low Cost and High Performance Polymer Donor Material for Polymer Solar Cells. *Nat. Commun.* **2018**, *9*, 743.

(47) Yuan, J.; Zhang, Y.; Zhou, L.; Zhang, G.; Yip, H.-L.; Lau, T.-K.; Lu, X.; Zhu, C.; Peng, H.; Johnson, P. A. Single-Junction Organic Solar Cell with over 15% Efficiency Using Fused-Ring Acceptor with Electron-Deficient Core. *Joule* **2019**, *3*, 1140.

(48) Stoltzfus, D. M.; Donaghey, J. E.; Armin, A.; Shaw, P. E.; Burn, P. L.; Meredith, P. Charge Generation Pathways in Organic Solar Cells: Assessing the Contribution from the Electron Acceptor. *Chem. Rev.* **2016**, *116*, 12920–12955.

(49) Singh, R.; Shivanna, R.; Iosifidis, A.; Butt, H.-J.; Floudas, G.; Narayan, K. S.; Keivanidis, P. E. Charge Versus Energy Transfer Effects in High-Performance Perylene Diimide Photovoltaic Blend Films. *ACS Appl. Mater. Interfaces* **2015**, *7*, 24876–24886.

(50) Grätzel, M. Dye-Sensitized Solar Cells. *J. Photochem. Photobiol., C* **2003**, *4*, 145–153.

(51) Zhang, C.; Choi, S.; Haliburton, J.; Cleveland, T.; Li, R.; Sun, S.-S.; Ledbetter, A.; Bonner, C. E. Design, Synthesis, and Characterization of a –Donor–Bridge–Acceptor–Type Block Copolymer via Alkoxy- and Sulfone-Derivatized Poly(phenylenevinylene)s. *Macromolecules* **2006**, *39*, 4317–4326.

(52) Sun, S.-S.; Zhang, C.; Ledbetter, A.; Choi, S.; Seo, K.; Bonner, C. E., Jr; Drees, M.; Sariciftci, N. S. Photovoltaic Enhancement of Organic Solar Cells by a Bridged Donor-Acceptor Block Copolymer Approach. *Appl. Phys. Lett.* **2007**, *90*, 043117.

(53) Lee, S. K.; Zu, Y.; Herrmann, A.; Geerts, Y.; Müllen, K.; Bard, A. J. Electrochemistry, Spectroscopy and Electrogenerated Chemiluminescence of Perylene, Terrylene, and Quaterylene Diimides in Aprotic Solution. *J. Am. Chem. Soc.* **1999**, *121*, 3513–3520.

(54) Howard, I.; Mangold, H.; Etzold, F.; Gehrig, D.; Laquai, F. *Ultrafast Dynamics in Molecules, Nanostructures and Interfaces*; World Scientific: Singapore, 2013.

(55) Stappert, S.; Li, C.; Müllen, K.; Basché, T. Synthesis of an Acceptor-Donor-Acceptor Multichromophore Consisting of Terrylene and Perylene Diimides for Multistep Energy Transfer Studies. *Chem. Mater.* **2016**, *28*, 906–914.

(56) Kim, H. N.; Puhl, L.; Nolde, F.; Li, C.; Chen, L.; Basché, T.; Müllen, K. Energy Transfer at the Single-Molecule Level: Synthesis of a Donor-Acceptor Dyad from Perylene and Terrylene Diimides. *Chem.—Eur. J.* **2013**, *19*, 9160–9166.

(57) Wolfs, M.; Delsuc, N.; Veldman, D.; Anh, N. V.; Williams, R. M.; Meskers, S. C. J.; Janssen, R. A. J.; Huc, I.; Schenning, A. P. H. J. Helical Aromatic Oligoamide Foldamers as Organizational Scaffolds

for Photoinduced Charge Transfer. *J. Am. Chem. Soc.* **2009**, *131*, 4819–4829.

(58) Goldsmith, R. H.; Sinks, L. E.; Kelley, R. F.; Betzen, L. J.; Liu, W.; Weiss, E. A.; Ratner, M. A.; Wasielewski, M. R. Wire-Like Charge Transport at near Constant Bridge Energy through Fluorene Oligomers. *Proc. Natl. Acad. Sci. U.S.A.* **2005**, *102*, 3540–3545.

(59) Tang, Y.; Hill, E. H.; Zhou, Z.; Evans, D. G.; Schanze, K. S.; Whitten, D. G. Synthesis, Self-Assembly, and Photophysical Properties of Cationic Oligo(p-phenyleneethynylene)s. *Langmuir* **2011**, *27*, 4945–4955.

(60) Candeias, L. P.; Grozema, F. C.; Padmanaban, G.; Ramakrishnan, S.; Siebbeles, L. D. A.; Warman, J. M. Positive Charge Carriers on Isolated Chains of MEH-PPV with Broken Conjugation: Optical Absorption and Mobility. *J. Phys. Chem. B* **2003**, *107*, 1554–1558.

(61) Li, N.; Jia, K.; Wang, S.; Xia, A. Theoretical Study of Spectroscopic Properties of Dimethoxy-P-Phenylene-Ethynylene Oligomers: Planarization of the Conjugated Backbone. *J. Phys. Chem. A* **2007**, *111*, 9393–9398.

(62) Ford, W. E.; Kamat, P. V. Photochemistry of 3, 4, 9, 10-Perylenetetracarboxylic Dianhydride Dyes. 3. Singlet and Triplet Excited-State Properties of the Bis (2, 5-Di-Tert-Butylphenyl) Imide Derivative. *J. Phys. Chem.* **1987**, *91*, 6373–6380.

(63) Gorczak, N.; Renaud, N.; Tarkuç, S.; Houtepen, A. J.; Eelkema, R.; Siebbeles, L. D. A.; Grozema, F. C. Charge Transfer Versus Molecular Conductance: Molecular Orbital Symmetry Turns Quantum Interference Rules Upside Down. *Chem. Sci.* **2015**, *6*, 4196–4206.

(64) Birks, J. B. *Photophysics of Aromatic Molecules*; Wiley, 1970.

(65) Morteani, A. C.; Sreearunothai, P.; Herz, L. M.; Friend, R. H.; Silva, C. Exciton Regeneration at Polymeric Semiconductor Heterojunctions. *Phys. Rev. Lett.* **2004**, *92*, 247402.

(66) Kamm, V.; Battagliarin, G.; Howard, I. A.; Pisula, W.; Mavrinskiy, A.; Li, C.; Müllen, K.; Laquai, F. Polythiophene: Perylene Diimide Solar Cells—the Impact of Alkyl-Substitution on the Photovoltaic Performance. *Adv. Energy Mater.* **2011**, *1*, 297–302.

(67) Fückel, B.; Köhn, A.; Harding, M. E.; Diezemann, G.; Hinze, G.; Basché, T.; Gauss, J. Theoretical Investigation of Electronic Excitation Energy Transfer in Bichromophoric Assemblies. *J. Chem. Phys.* **2008**, *128*, 074505.

(68) Holcombe, T. W.; Norton, J. E.; Rivnay, J.; Woo, C. H.; Goris, L.; Piliago, C.; Griffini, G.; Sellinger, A.; Brédas, J.-L.; Salteo, A.; Fréchet, J. M. J. Steric Control of the Donor/Acceptor Interface: Implications in Organic Photovoltaic Charge Generation. *J. Am. Chem. Soc.* **2011**, *133*, 12106–12114.

(69) Labrunie, A.; Gorenflot, J.; Babics, M.; Alévêque, O.; Dabos-Seignon, S.; Balawi, A. H.; Kan, Z.; Wohlfahrt, M.; Levillain, E.; Hudhomme, P.; Beaujuge, P. M.; Laquai, F.; Cabanetos, C.; Blanchard, P. Triphenylamine-Based Push-Pull  $\sigma$ -C60 Dyad As Photoactive Molecular Material for Single-Component Organic Solar Cells: Synthesis, Characterizations, and Photophysical Properties. *Chem. Mater.* **2018**, *30*, 3474–3485.

(70) Deshmukh, K. D.; Prasad, S. K. K.; Chandrasekaran, N.; Liu, A. C. Y.; Gann, E.; Thomsen, L.; Kabra, D.; Hodgkiss, J. M.; McNeill, C. R. Critical Role of Pendant Group Substitution on the Performance of Efficient All-Polymer Solar Cells. *Chem. Mater.* **2017**, *29*, 804–816.

(71) Tauler, R.; Smilde, A.; Kowalski, B. Selectivity, Local Rank, Three-Way Data Analysis and Ambiguity in Multivariate Curve Resolution. *J. Chemom.* **1995**, *9*, 31–58.

(72) de Juan, A.; Jaumot, J.; Tauler, R. Multivariate Curve Resolution (Mcr). Solving the Mixture Analysis Problem. *Anal. Methods* **2014**, *6*, 4964–4976.

(73) Miertuš, S.; Scrocco, E.; Tomasi, J. Electrostatic Interaction of a Solute with a Continuum. A Direct Utilization of Ab Initio Molecular Potentials for the Prediction of Solvent Effects. *Chem. Phys.* **1981**, *55*, 117–129.

(74) Cossi, M.; Barone, V.; Cammi, R.; Tomasi, J. Ab Initio Study of Solvated Molecules: A New Implementation of the Polarizable Continuum Model. *Chem. Phys. Lett.* **1996**, *255*, 327–335.

(75) Tomasi, J.; Mennucci, B.; Cammi, R. Quantum Mechanical Continuum Solvation Models. *Chem. Rev.* **2005**, *105*, 2999–3094.

(76) Frisch, M.; Trucks, G.; Schlegel, H.; Scuseria, G.; Robb, M.; Cheeseman, J.; Scalmani, G.; Barone, V.; Mennucci, B.; Petersson, G. A.; Farkas, O.; Foresman, J. B.; Ortiz, J. V.; Cioslowski, J.; Fox, D. J. *Gaussian*, 2009; Vol. 9, pp 1372–1377.